Plasma formation in metallic wire Z pinches

J. P. Chittenden, S. V. Lebedev, J. Ruiz-Camacho, F. N. Beg, S. N. Bland, C. A. Jennings, A. R. Bell, and M. G. Haines

Blackett Laboratory, Imperial College, London SW7 2BZ, United Kingdom

S. A. Pikuz and T. A. Shelkovenko

P. N. Lebedev Physical Institute, Moscow 121433, Russia

D. A. Hammer

Laboratory of Plasma Studies, 369 Upson Hall, Cornell University, Ithaca, New York 14853

(Received 29 October 1999)

Plasma formation in metallic wire Z pinches is modeled using a two-dimensional resistive magnetohydrodynamics code. Modified Thomas-Fermi equations of state and dense plasma transport coefficients allow the phase transitions from solid to plasma to be approximated. Results indicate the persistence of a two-component structure with a cold, dense core embedded within a much hotter, low density, $m=0$ unstable corona. Extensive benchmark testing against data from a number of single-wire experiments is presented. Artificial laser schlieren and x-ray back-lighting images generated from the code data are compared directly to experimental results. The results were found to be insensitive to inaccuracies in the equations of state and transport coefficients. Simulations of individual wires in a wire array show different behavior to that observed experimentally due to the absence of three-dimensional effects. Simulations with similar conditions to wires in an array show a general trend in the plasma structure at start of implosion from discrete wires with large $m=0$ perturbation amplitudes to partially merged wires with smaller perturbation amplitudes as the number of wires is increased. Results for a wire number scan with aluminum wire arrays on the SATURN generator suggest that the observed sharp transition to high x-ray power at around 40 wires corresponds to a sharp decrease in $m=0$ perturbation amplitude and hence a sharp decrease in the seed perturbation for the Rayleigh-Taylor instability.

PACS number(s): 52.55.Ez, 52.65.−y, 52.35.−g, 51.30.+i

I. INTRODUCTION

The recent spectacular improvements in x-ray power attained in Z-pinch implosions [1–4] are generally attributed to the improved plasma uniformity obtained with wire arrays compared to other loads. In addition, the apparently continuous improvements obtained by using ever larger numbers of finer wires has led to load designs with as many as 480 fine tungsten wires. The development of this technique has however been, to date, largely empirical. One reason for this is the absence of detailed theoretical models to describe the transition from discrete solid wires into an imploding plasma ensemble.

At first sight, determining the time at which complete vaporization and ionization of such wires occurs seems to be a simple matter of calculating the rate of energy deposition into the wire material. Consider 2 cm long, 7.5 μm diameter tungsten wires with current rising in each wire at 1 kA per nanosecond (parameters that are typical of many wire array experiments). Since the skin depth greatly exceeds the wire radius, Ohmic heating of the wire is at first volumetric. Using the resistivity model described below, the 78 mJ required to heat the wire material to the vaporization temperature and provide the latent heats of fusion and evaporation is deposited in the first 0.75 ns. To deposit the further 83 mJ required to heat the material to ionization temperatures and provide the first ionization energy takes a further 0.15 ns. Therefore, compared to the 100 ns time scale of the current rise, we would expect the entire array mass to become plasma almost

instantaneously. This scenario does not, however, take into account the inhomogeneity with which phase transitions occur. Once the surface vapor starts to expand into the vacuum, its density drops and hence this is where ionization first occurs forming a low-density plasma corona. Whilst the resistivity of this plasma is comparable to that of the liquid/vapor core, the cross-sectional area of the corona is much greater than that of the core and hence the majority of the current is switched to the corona. Since the density and therefore the specific heat capacity of the corona are low, Ohmic heating results in a rapid temperature rise and fast expansion of surface plasma. Therefore, within a few nanoseconds of current start, the region of energy deposition has been moved away from the reservoir of cold core material. Any further ionization of the core material relies on the diffusion of thermal energy and magnetic flux from the corona into the core. Since the time scale for diffusion can be a significant fraction of the current rise time, the liquid/vapor core ionizes slowly and can persist until late into the discharge.

Numerous experiments in both single wires [5–12] and in wire arrays [13–15] have observed this two-component structure with a low-density plasma corona surrounding a much higher density core that persists until late into the discharge. In wire array Z-pinch experiments the coronal plasma is swept around the stationary wire cores forming radial plasma streams, which reach the axis at roughly half the final implosion time forming a precursor plasma [14–18]. Two-dimensional (2D) simulations of such experiments in the r-θ plane [19] can reproduce the observed behavior by

initially approximating the core as a high-density neutral gas. This insulating medium then remains force free and stationary until finally disappearing just prior to the final implosion. In addition, these experiments exhibit substantial $m=0$ instability growth in the plasma surrounding the individual wire cores, prior to the main implosion. The statistical average [20] of these perturbations is the most likely source of seed perturbation for the global magneto-Rayleigh-Taylor (MRT) instability observed during final implosion. The MRT instability is at present thought to be the primary mechanism for broadening the imploding plasma annulus and hence determining the x-ray power attained at stagnation.

In this paper, we describe the detailed modeling of single metallic wires driven by large, fast rising currents. A 2D(r,z) resistive magnetohydrodynamics (MHD) code [21] is used with the addition of dense plasma transport coefficients [22] and modified Thomas-Fermi equations of state, which allow the phase transitions from solid to plasma to be approximated. Extensive benchmark testing against data from a number of single-wire experiments is presented. Artificial laser schlieren and x-ray back-lighting images generated from the code data are compared directly to experimental results. The 2D(r,z) simulations of individual wires presented here cannot model the complex 3D behavior of wire arrays in which the MRT instability present in the r-z plane is superimposed on a modulated structure in the r-θ plane provided by the wires. We can, however, describe the extent of core expansion, ionization and $m=0$ instability in both corona and core for single wires under similar conditions to those in an array, at times corresponding to the start of global implosion. From these data we can then infer the dependence of the structure of the imploding plasma ensemble and most critically the seed perturbation for the MRT as functions of the number of wires.

II. MODEL

The model is based on the 2D(r,z) resistive MHD code described in Refs. [21] and [23]. Explicit hydrodynamics is performed on an Eulerian grid using second order Van Leer advection (as interpreted by Youngs [24]). Reflective boundary conditions are used at the axial boundaries and at the pinch axis with free flow conditions at the outer radial boundary. The thermal and magnetic-field diffusion equations are backwards differenced and solved implicitly by quin-diagonal matrix solution using the incomplete Cholesky conjugate gradient iterative method of Kershaw [25]. The model is two temperature, with separate electron and ion energy equations coupled by an equilibration term. A simple optically thin radiation loss model [26,27] is modified to include a probability of escape, which allows a smooth transition to black-body emission in the core and the adjacent plasma.

Material with a mass density below $10^{-4}\,\mathrm{kg\,m^{-3}}$ is labeled vacuum and given artificially high resistivity and thermal conductivity in order to ensure that this region remains current free and isothermal. As with all other free parameters in the model the choice of vacuum cut-off density was arrived at by trial and error, running the code many times and reducing the value until no further change in results (primarily the evolution of radius and wavelength) was observed.

The choice of such a low cut-off density allows unphysical conditions to arise where the electron drift velocity greatly exceeds the local ion sound speed. Under such conditions lower hybrid microinstabilities grow rapidly and saturate resulting in an anomalously high electron-ion collision frequency. The inclusion of an anomalous component to the electron-ion collision frequency in the evaluation of electrical resistivity and electron thermal conductivity, serves to limit the electron drift velocity to less than the ion sound speed, provides a physically justifiable scaling from finite plasma resistivity to virtually infinite vacuum resistivity and prevents a large discontinuity in transport coefficients at the vacuum/plasma boundary [28]. Whilst the inclusion of anomalous resistivity due to the lower hybrid drift microinstability does affect the expansion rate and instability growth in the lowest density regions of the corona it does not have as strong an effect in this work as in other work [28,21].

The results presented here use grids with 150 axial cells each 30 μm long, i.e., with a grid length of 4.5 mm. These sizes were arrived at empirically by running the code exhaustively for a large number of different conditions and reducing the axial cell length and increasing the number of axial cells until no further change in results was observed. The results detailed below exhibit minimum wavelengths of 150–250 μm indicating that 5–8 cells per wavelength are required for complete resolution. The longest wavelengths modeled below are ~2 mm. The grid length of 4.5 mm thus includes a safety margin that allows the simulation to grow longer wavelengths if required.

The radial width of cells is set to 1.25 μm near the axis to allow the solid wire to be resolved and increases with radius becoming 30 μm square at 250 μm. The long aspect ratio of cells near the axis suggests that advection of material in diagonal directions across such cells will be inaccurate. However, this does not appear to affect the growth of the instability, which occurs almost entirely out in the corona where the cells are square. In order to minimize runtime for the calculations, the number of radial cells is increased or decreased so that the boundary of the problem is always 10 cells away from the largest vacuum/plasma boundary radius.

Instability growth is seeded with a $\pm 0.1\%$ random density perturbation. Since the instability rapidly enters a nonlinear stage of development the results after the first 15 ns are insensitive to the perturbation amplitude.

III. EQUATIONS OF STATE

During the solid and liquid phases, the wire material remains virtually stationary and holds together. At the vaporization temperature of aluminum, the pressure of a perfect gas at solid density is ~20 kbar. The electrons in this material do not, however, behave as a perfect gas. In condensed phases, exchange effects act as a binding force so that little or no pressure is exerted by the electrons. Even in the vapor state, at high enough densities and low enough temperatures, the pressure and internal energy of the electron fluid are substantially reduced with respect to the perfect gas values. The behavior of the condensed states of matter can be emulated in a fluid simulation by modifying the equations of state to include degeneracy, nuclear potential and exchange effects. In the work presented here, we use analytic approximations
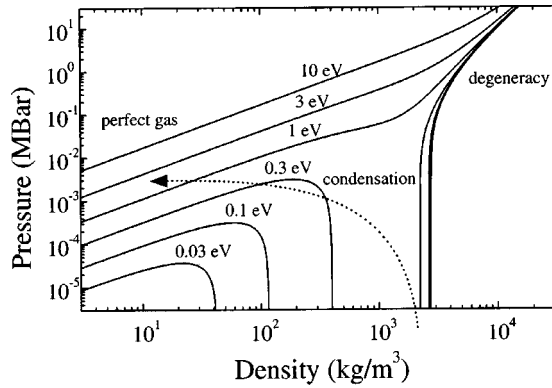
FIG. 1. Electron pressure versus density for various temperatures provided by the equation of state model. A typical trajectory (······), for material ablated from the core and expanding out into the corona, is shown.

FIG. 2. Approximation to the IMP generator current versus time used in simulations.

to Latter's results [29] for a Thomas-Fermi model of the electrons to determine the internal energy, pressure and energy derivatives ($\partial U/\partial T$ and $\partial U/\partial \rho$) as functions of the density and temperature. Corrections to include quantum and exchange effects [30] then allow the condensed phases to be modeled. This equation of state model was originally developed by one of the authors (ARB) in 1980 and been used extensively in the 1D Lagrangian laser-plasma hydrodynamics code MEDUSA [31].

Figure 1 shows the electron pressure in aluminum calculated by this model as a function of density, for various temperatures. At high temperatures and low densities, the straight line dependence is indicative of perfect gas behavior. At very high densities the pressure is increased over the perfect gas value, eventually becoming a function of density only as the electrons become degenerate. For low temperatures around solid density, the electron pressure becomes negative, thus modeling a condensed phase. In practice the ions are still treated with the perfect gas equation of state and a minimum electron pressure is set so that the minimum total pressure is zero. The model represents a generic equation of state with no knowledge of the details of each phase transition and how these differ with material. The solid density of the material is, however, used as an input parameter in order to establish the relative importance of the correction terms. Comparison to the Los Alamos SESAME database indicates good agreement in general, however, the analytic approximations used become inaccurate at very low temperatures and densities.

Material ablated from the core and expanding out into the corona emerges from the condensed phase towards the perfect gas regime, following a trajectory similar to the example superimposed on Fig. 1, with degeneracy playing little part in the problem.

The strong gradients in Fig. 1 mean that small changes in density and temperature can result in large pressure changes. Using the value of $\partial U/\partial \rho$ returned by the equation of state model to determine the sound speed and hence the time step, usually eliminates numerical instabilities. If, however, the problem is initialized with too large a discontinuity in density between the last cell containing wire material and the first vacuum cell, then the first motion of this interface tends to excite gross fluctuations in the density and pressure. To
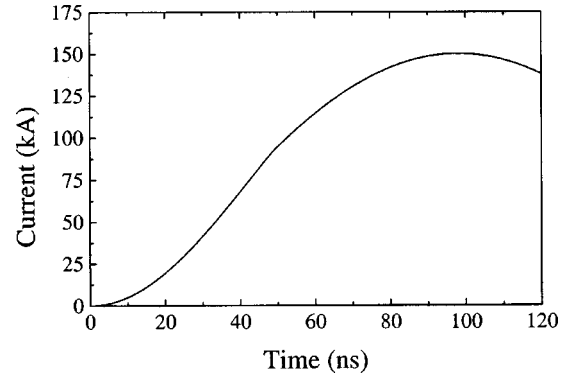
prevent this a small amount (~0.01% of the mass of the wire) of gaseous material is placed just outside the wire to provide sufficient pressure to prevent gross motion of the material/vacuum interface during the first nanosecond. The width of this gaseous region is set to be the same as the wire radius with the density falling off gradually to reach vacuum. The current initially flows in the solid wire and bypasses the gaseous region, which therefore has little effect other than providing numerical stability.

IV. TRANSPORT COEFFICIENTS

In order to calculate the diffusion of magnetic field, the energy deposition by Ohmic heating and energy transfer by thermal conduction, it is essential to include accurate electrical resistivities and thermal conductivities that span a wide range of different material parameters and states. At low temperatures, the resistivity of the solid and liquid phases of metals and their rate of increase with temperature is well established [32]. In the high temperature and low density well-ionized plasma limit, the resistivity of plasma adopts the well established Spitzer-like dependence of $T^{-3/2}$. Between these two well-established limits, around the implied resistivity maximum at $1-10$ eV, there is considerable uncertainty (particularly at densities lower than solid) with more than an order of magnitude difference between theoretical models. For this paper, we adopt a model based on the dense plasma electron conductivity model of Lee and More [22]. The electron mean free path used to calculate the electron relaxation time in the condensed phase [Eqs. (32) and (33) in Ref. [22]], is modified to include a different minimum temperature for each metal used. This provides a mechanism for numerically fitting the resistivity model to the known behavior [32] at low temperature and solid density and results in somewhat higher resistivities in the condensed phases than in Ref. [22].

V. EXAMPLE RESULTS IN 1D

The evolution of the wire/plasma structure is best illustrated qualitatively in the absence of additional complexity of instabilities detailed below, i.e., in one dimensional (radial) simulations. As an example, we consider 15 μm aluminum wires driven by the IMP generator (150 kA, 480 kV, 65 ns 10–90% current rise time) at Imperial College. Figure 2 shows the approximation to the experimental current wave-
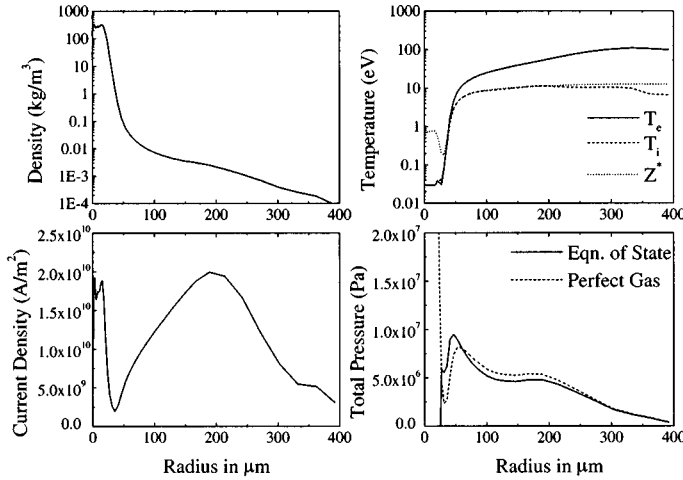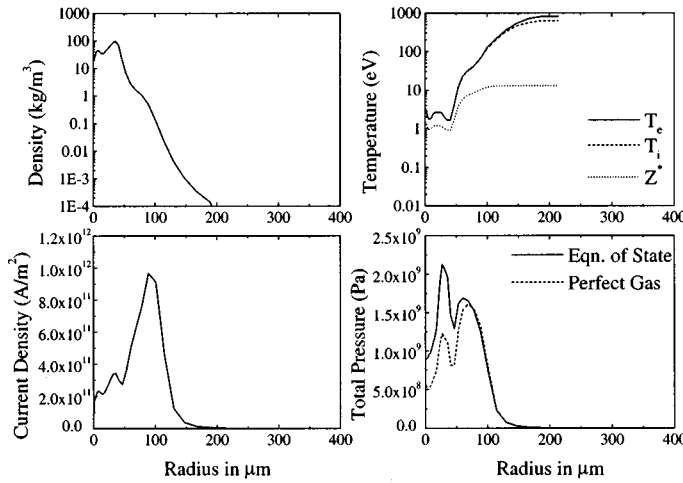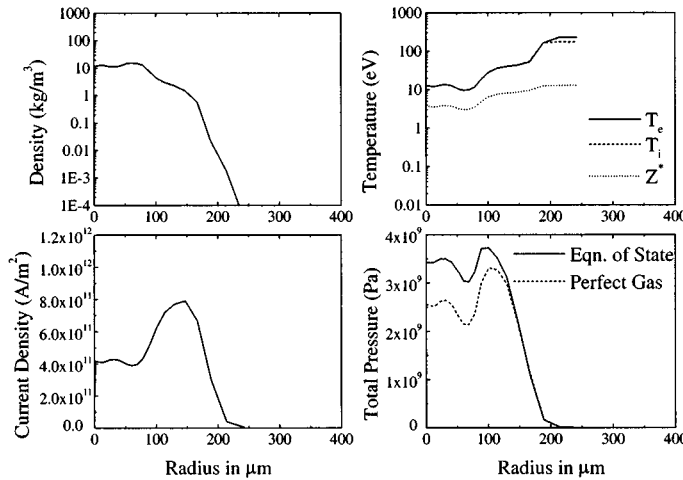
FIG. 3. Radial profiles from a 1D (r) simulation of a 15 μm aluminum wire on the IMP generator at (a) 10 ns, (b) 25 ns, and (c) 40 ns.

form used in simulations. With an average dI/dt of 2 $\times 10^{12}$ A s^{-1}, this current is comparable to the current per wire in array implosions on the SATURN and Z generators.

During the first 3.5 ns the wire temperature gradually increases up to roughly the vaporization temperature. During this period the total pressure in the wire material is negligible and therefore the material remains stationary. Once the temperature is sufficient for the pressure to be finite and positive, the wire material begins to expand. Ionization first occurs in the lowest density surface regions forming the plasma corona. Figure 3(a) shows the radial profiles after 10 ns, with a well-established two component structure of a hot, low-density corona surrounding a cold, high density core. Initially the core expands at roughly the sound speed of aluminum at its vaporization temperature and therefore by 10 ns the core has expanded threefold and its density has dropped
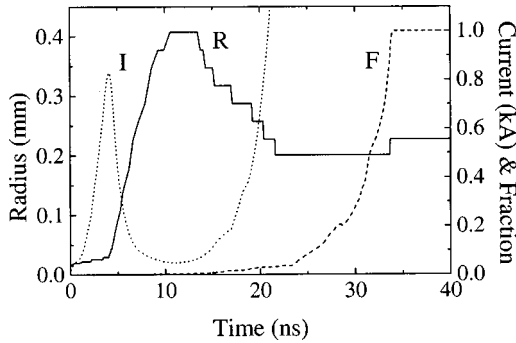
FIG. 4. Radius of the vacuum/plasma boundary, fraction of mass not in a condensed phase and current in the core versus time from a 1D (*r*) simulation of a 15 μm aluminum wire on the IMP generator.

FIG. 5. A series of mass density contour maps from a 2D (*r,z*) simulation of a 15 μm aluminum wire on the IMP generator.

by an order of magnitude from solid density. The expansion also cools the electrons and ions back down to roughly room temperature, which means that the pressure drops to much less than the perfect gas value, thereby reducing the rate of core expansion and keeping it intact. Despite the low temperature, the density in the core is sufficiently high for the material to have a large population of free electrons and therefore the resistivity is low and the current density is high. However, the small cross-sectional area of the core compared to that of the corona, means that only 1.5% of the total current flows in the core. Since the corona represents less than 1% of the mass of the wire during this phase, the presence of such a large fraction of the current rapidly heats the surface plasma to $\sim$50 eV. As a result, the phase transition to vapor and the first formation of surface plasma which occurs at 3.5 ns is followed by unconfined, ballistic expansion of the surface plasma at the sound speed ($\sim$5$\times$10^4 ms^{-1} for aluminum at 50 eV). At 10 ns, the magnetic field becomes sufficient to confine the coronal plasma, rapid expansion ceases and self-pinching begins.

Figure 4 shows the self-pinching of the corona as illustrated by the trajectory of the vacuum/plasma boundary. Compression of the corona material onto the surface of the core triggers a rapid increase in the fraction of wire material liberated from the condensed phase which prior to this time remained at 1% or less. The definition of a condensed phase is somewhat arbitrary for this particular model and is here taken to represent any material where the electron pressure is significantly depressed with respect to the perfect gas value. Analysis of the various heating and cooling rates occurring in the simulation indicate that this rapid increase is the result of Ohmic heating in the wire core. Figure 4 also shows the current in the core as a function of time. For the first 3.5 ns the current flows in a solid wire. Following the formation of a conducting plasma corona, the core current gradually drops as current is shunted into the corona. At 10 ns, the corona has expanded to $\sim$400 μm radius and has a resistivity of $\sim$10^{-5} Ω m. The time-scale for magnetic-field penetration through the corona is therefore $\sim$60 ns and hence the core is magnetically isolated from the rest of the system. The core current therefore remains crowbarred at $\sim$100 A until self-pinching of the corona allows further magnetic-field penetration and the current increases rapidly.

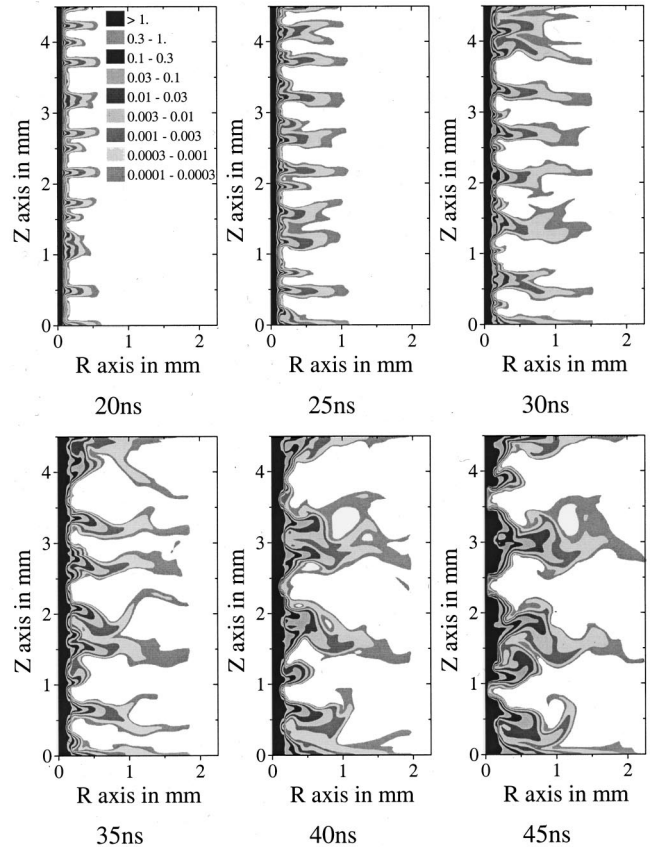Figure 3(b) shows the radial structure just after self pinch-

ing at 25 ns. The corona has been compressed onto the surface of the core, 6% of the current is now flowing in the core which is sufficient to Ohmically heat the core material to $\sim$2 eV. As the core temperature rises, so does its resistivity and therefore the Ohmic heating rate escalates. The core continues to expand at roughly the sound speed (at this point $\sim$2500 ms^{-1} for ionization level $\sim$1 and $T_e \sim$2 eV). The density has dropped and the temperature increased sufficiently for the pressure to be close to the perfect gas value throughout the pinch (see Fig. 1). Figure 3(c) shows the structure after 40 ns, the core temperature and ionization level continue to increase slowly as a result of Ohmic heating. The core continues to expand, decelerating slowly in the presence of a negative pressure gradient. The corona retains the majority of current and in this one dimensional result, remains compressed onto the surface of the core. Whilst the condensed phases of core behavior are long gone by this time, the majority of the mass (80% lies within 100 μm of the axis) remains in a cold, dense object which is held in check by the higher pressure of the much hotter and more ionized corona.

Experience of single wire Z-pinch experiments suggests that the presence of $m=0$ MHD instabilities result in a substantial reduction in plasma confinement compared to Fig. 3(c). During self pinching, the Alfvén transit time across the corona drops from $\sim$50 ns at 10 ns to $\sim$5 ns at 20 ns. We would therefore expect self pinching to trigger rapid instability growth with the radial structure illustrated in Fig. 3(c) being representative only of the neck regions of the instability.
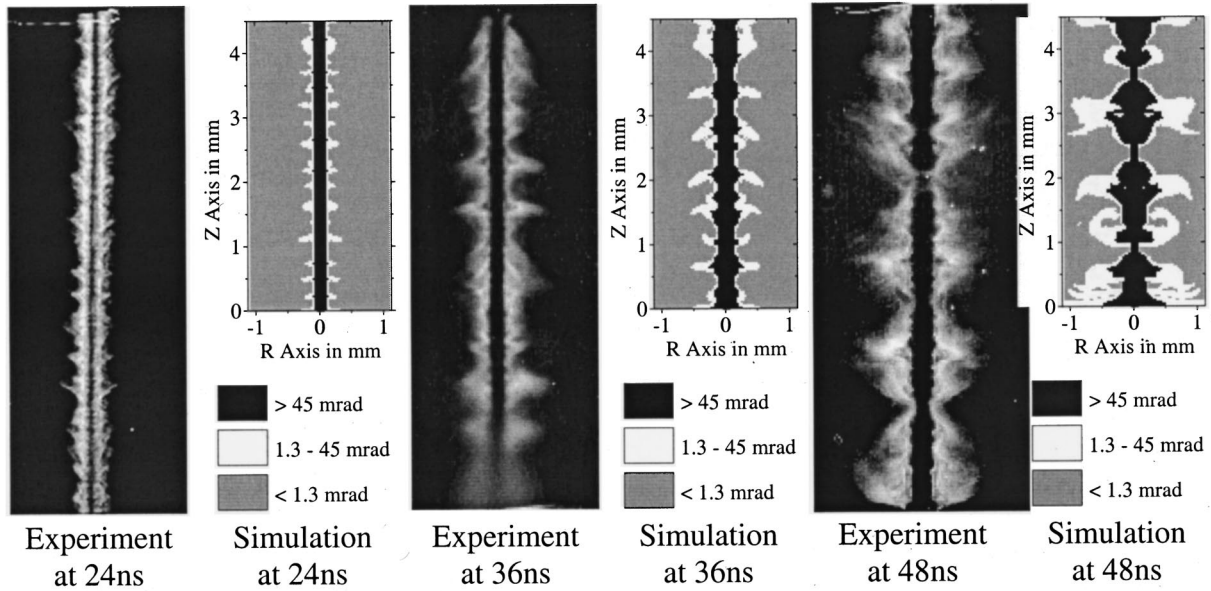
FIG. 6. Experimental and simulated laser Schlieren images for a 15 μm aluminum wire on the IMP generator.

VI. EXAMPLE RESULTS IN 2D

Figure 5 shows a series of mass density maps from a 2D simulation of the same test problem of one 15 μm aluminum wire on the IMP generator. $m=0$ instabilities are evident from $\sim$15 ns onwards, initially with $\sim$300 μm wavelength, evolving to longer wavelengths as the plasma expands, so that the wavelength divided by the radial scale length remains approximately constant. Rather than following a contorted path in and out of the radial ''flares'' or ''bulges'' of the instability, the current prefers to flow in the first available straight line path, i.e., just outside the core. As a consequence the flares of the instability are force free and almost completely unconfined and continuously expand at roughly the sound speed. Initially, the ''necks'' of the instability fail to penetrate the core which remains almost unperturbed. Some necks apparently ''bifurcate'' (as described in Refs. [33] and [21]) into two separate necks moving away from each other in the axial direction. During the first 40 ns, despite the instability the structure remains consistent with the one-dimensional results described above. The majority of the low density corona remains at 10–100 eV with the much high density and lower temperature core remaining intact and expanding slowly. At 45 ns the first penetration of an $m=0$ neck into the core occurs. Since the current is now constricted to flow in a very narrow region near the axis, the electron temperature in this neck reaches several hundred eV. The action of the $m=0$ instability therefore serves to bring the current and hence the high temperatures from the low-density coronal region down to the high-density core, resulting in a small ($\sim$100 μm) region that is simultaneously hot and dense and is therefore an intense source of soft x-rays. Experimental observations suggest that the bright-spots observed in x-ray streak photographs are coincident with the penetration of the core by the necks of the instability observed in laser schlieren photographs [11]. Despite the penetration of the core by the neck, the vast majority of the length of the core remains intact.

The very high Alfvén and sound speeds in the neck regions and the large extent of the computational grid caused by coronal expansion made the simulation of the late time behavior of the experiment computationally prohibitive. The simulation was therefore terminated after 50 ns.

VII. COMPARISON WITH EXPERIMENTS

The simulation and the theoretical models therein were bench tested by extensive comparison to experimental data from diagnostics, which probe both the corona and core plasmas. This process was facilitated by post processing the simulation results to generate ''artificial'' diagnostic images which can be compared directly with the experimental data.

A. Laser schlieren photography of IMP experiments [11]

Figure 6(a) shows three experimental laser Schlieren images from different discharges into 15 μm aluminum wires on the IMP generator (as modeled in the last two sections). A 7 ns full width at half maximum (FWHM) pulse of Ruby laser (694.3 μm) is used with a 520 μm circular stop. Gradients in refractive index (a function of electron density and laser wavelength) deviate the laser light on its passage through the plasma. Only light with refraction angles between 1.3 and 45 mrad (determined by the size of the stop and the diagnostic aperture, respectively) reaches the detector, thus providing two diagnostic cut-off contours, one in the low-density corona and one in the high-density plasma adjacent to the core. Using a similar method to Ref. [21], a contour map of deviation angle was constructed from the simulation data by integrating the perpendicular gradients in refractive index along all chords crossing the two-dimensional grid. Whilst this method is valid for small deviation angles ($<$10 mrad), strictly speaking, for higher deviation angles, it is necessary to follow the trajectory of laser light through the plasma using a ray tracing technique. In practice, however, the gradients of electron density adjacent
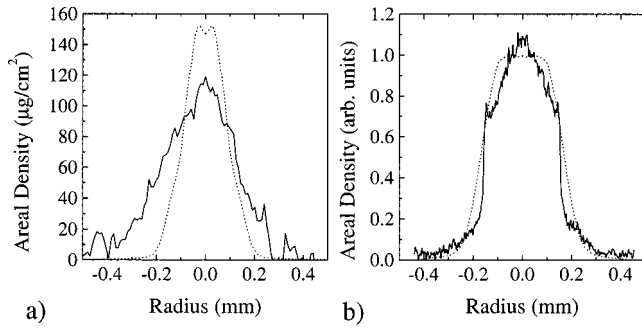
FIG. 7. Experimental (——) and simulated (······) areal density profiles from x-ray backlighting of (a) a 13 μm aluminum wire with 2.6 kA after 140 ns and (b) a 40 μm copper wire with 83 kA after 53 ns.

to the core are sufficiently high for the error in deviation angle as a function of radius to be relatively small. Absorption of the laser by inverse bremsstrahlung is also calculated along chord lengths. Significant absorption is only found to occur at smaller radii than the 45 mrad cut-off contour and therefore refraction is thought to be the only important process in determining the appearance of the simulated images in Fig. 6.

A visual comparison of experimental and simulated images shows good agreement at early times. More quantitatively, the corona minimum and maximum radii and the instability wavelengths agree to within 20% throughout the first 50 ns. In addition, the initial coronal expansion and self pinching illustrated in Fig. 4 can also be seen in the trajectory of the 1.3 mrad contour, which reproduces the behavior of Fig. 7 of Ref. [11]. The delay between the start of current flow and the onset of significant x-ray emission, core expansion, and instability development (often referred to experimentally as the ''dwell time'') is reproduced in simulation and corresponds to the self-pinching time of the corona. The expansion of the core is, however, noticeably faster in simulation than in experiment. In addition (and probably as a

consequence of this expansion), the core exhibits a greater susceptibility to penetration by the instability in simulation and therefore the late time agreement between simulation and experiment is not as good as at early times.

B. Soft x-ray back lighting of Cornell University Z-pinch experiments

With a maximum acceptance angle of 45 mrad, the plasma probing by optical lasers is limited by refraction to electron densities of $\sim 10^{26}$ m^3 or lower. Probing with shorter wavelength, soft x-ray radiation allows diagnosis of much higher density regions of the core plasma. References [12] and [34] describe the use of molybdenum X pinches to generate a short (0.7–2 ns) burst of soft (2–6 keV) x rays and how this can be used to produce absorption radiographs of high-density, single-wire Z-pinch experiments. Since the energy of the probing radiation greatly exceeds the plasma temperature in the dense core, the absorption process is the same as in solid aluminum. Therefore, the optical film density in x-ray back-lighting images can be compared directly to that obtained using an aluminum coated step wedge during the same shot to give absolute measurements of areal density. These data can then be compared to integrals of mass density along chords ($\int \rho \, dl$) through the 2D(r,z) simulation grid. Figure 7 shows a comparison of simulated and experimental areal density profiles for two very different Z-pinch experiments (a 13 μm aluminum wire with 2.6 kA after 140 ns and a 40 μm copper wire with 83 kA after 53 ns). In both cases the level of $m=0$ instability imprint on the core at the time of diagnosis was negligible. In contrast to the simulation of IMP experiments described above, the simulation of the low current, aluminum wire predicts slightly less core expansion than observed experimentally. Absolute measurements of areal density are not available for the copper experiment and therefore the ordinates in this graph have been self normalized to provide the best apparent fit with the simulation. The size of the core, however, is in good agreement.
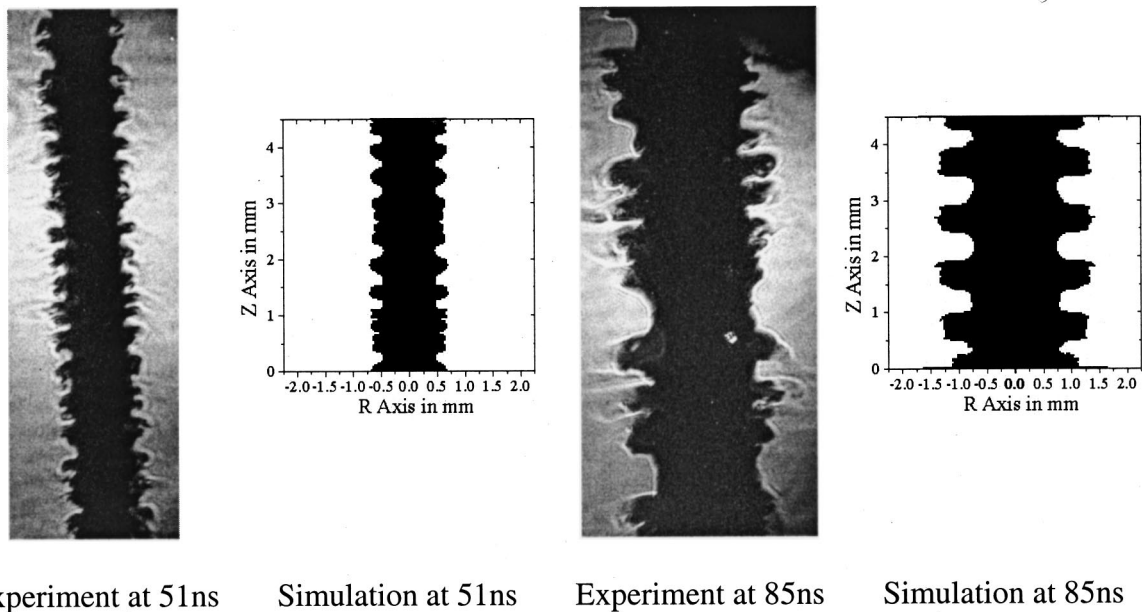

Experiment at 51ns   Simulation at 51ns   Experiment at 85ns   Simulation at 85ns

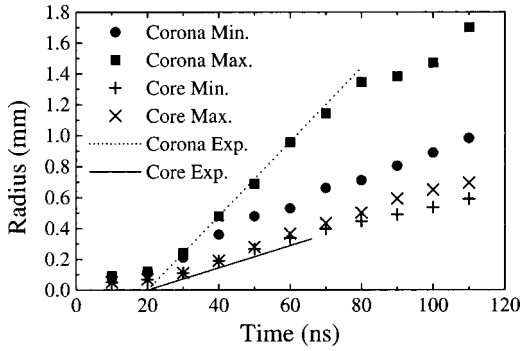FIG. 8. Experimental and simulated laser schlieren images for a 100 μm aluminum wire on the Cornell generator at 51 and 85 ns.

FIG. 9. Comparison of experimental and simulated core and corona expansion velocities for a 100 μm aluminum wire on the Cornell generator.

C. Simultaneous laser schlieren and soft x-ray back lighting [6]

The most severe test of the code comes from testing its ability to reproduce the behavior of both core and coronal plasma simultaneously in the same experiment. Experimental test data for this comes from Ref. [6] in which a subnanosecond, 337 nm, nitrogen laser and X pinches consisting of various wire materials were used to probe 100 μm aluminum wire Z-pinches (driven by a 100 ns, 145 kA current) at various times in different discharges. In the schlieren system, a pinhole obscured all laser light with a deviation angle greater than ~10 mrad providing a single cut-off contour in the higher density regions of the corona. Whilst the x-ray backlighting images obtained in this experiment were not absolutely calibrated, the contrast in film density shows a steep gradient at the core/corona boundary, which means that the apparent core radius can be readily identified from the simulated $\int \rho \, dl$. Figure 8 shows a visual comparison of the experimental and simulated laser schlieren images indicating good agreement. The large wire size means that the $m=0$ instability is not visible in the back-lighting images as it does not begin to imprint on the wire core until ~70 ns and does not penetrate through the core at all during the current rise time. Figure 9 shows a comparison of the experimental core and corona expansion velocities with points taken from the simulated diagnostic images. For each simulated diagnostic a minimum and maximum radius is shown corresponding to the necks and bulges of the $m=0$ instability. In contrast to the IMP experiments described above, the delay in the ex-

pansion of both the corona and core is the time taken to heat this massive wire to the vaporization temperature.

VIII. RELEVENCE TO WIRE ARRAY Z-PINCH EXPERIMENTS

Having demonstrated that the model can reproduce most of the behavior of single wire experiments it then becomes interesting to use this model to describe the ablation and instability behavior of a single wire in a wire array Z pinch. It must however be stressed that the following results should be considered qualitatively, since experimental data for wire arrays [14,15] clearly indicates that the magnetic-field geometry results in a noncircular plasma cross section that modifies the evolution of the ablation and instability compared to single wire experiments.

Figure 10 shows mass density contour maps for one of 16, 15 μm aluminum wires on the MAGPIE generator, one of 24, 25 μm aluminum wires on the SATURN generator, one of 64, 15 μm aluminum wires on the SATURN generator and one of 240, 7.5 μm tungsten wires on the Z generator. In each case the results are plotted at the beginning of the implosion phase at a time when the equation of motion for the array suggests that the wires have moved 5% from their original radial position (8 mm for MAGPIE, 8.6 mm for SATURN, and 20 mm for Z). In each case in Fig. 10, a dense wire core retains the majority of the mass within a few hundred microns of the axis and persists at least up until the time at which global implosion would start. In the case of 24, 25 μm aluminum wires on the SATURN generator, in which the current per wire is by far the largest, the $m=0$ instability development in the corona is sufficient to penetrate the core (see below). In the three other cases, the dense core and hence the majority of the mass remain unperturbed at this time.

The discrepancy between the single wire behavior of these simulations and the instability behavior of wires in an array becomes readily apparent when comparing Fig. 10(a) with the laser probing images in Refs. [14] and [15]. In simulation, the average wavelength of the instability increases continuously as the corona expands (as in Sec. VI) reaching several mm at the beginning of the implosion. In experiments, coronal plasma liberated from the wire cores is accelerated towards the common axis in the form of radial plasma streams. The plasma cross section around each wire is highly noncircular with the effective ''radius'' having a different

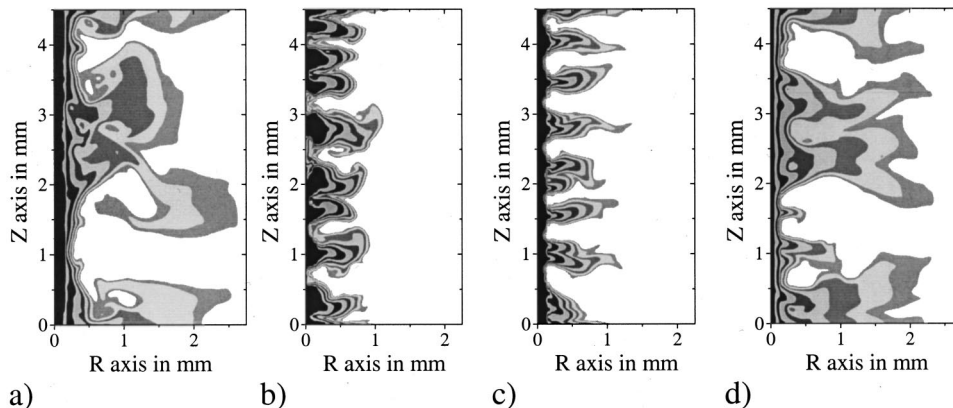a)   b)   c)   d)

FIG. 10. Mass density contour maps (contours as in Fig. 5) for (a) 16×15 μm aluminum wires on MAGPIE, (b) 24×25 μm aluminum wires on SATURN, (c) 64×15 μm aluminum wires on SATURN, (d) 240×7.5 μm tungsten wires on Z.

evolution to that of a single wire. The instability exhibits an almost constant ~0.5 mm wavelength from early times right up until final implosion. The structure of this 0.5 mm mode is highly periodic, implying a much narrower spectrum of wavelengths than in single wires Z pinches. The applications of the simulation to modeling wire array Z-pinch experiments are therefore limited to establishing trends in behavior as functions of the wire material and the current per wire.

A. Scaling with the number of wires in an array

A wide variety of experimental data suggest that the degree of implosion symmetry and hence the peak x-ray power obtained, can be improved by keeping the total implosion mass constant and using larger numbers of finer wires. A particularly marked example of this is the case of aluminum wire arrays [1,35] on the SATURN generator which showed a transition in the dependence of x-ray power upon wire number at around 40 wires (corresponding to a 1.4 mm interwire gap for an 8.6 mm radius array).

Two obvious mechanisms for broadening the imploding plasma shell and hence broadening the x-ray pulse rise time are, the injection of mass between the wires into the interior of the array during the plasma formation phase and the development of a 3D magneto-Rayleigh-Taylor instability during the implosion phase. Whilst we cannot address either of these phenomena directly using this model, we can investigate the ablation, expansion and instability development in individual wires (which are responsible for their development) and examine how the magnitudes of these effects vary with the number of wires. In the 2D(r,z) results presented here, which do not include the effects of interaction between neighboring wire plasmas and the global magnetic field, scaling with the number of wires simply equates to scaling with the current per wire.

Simulations of single aluminum wires were conducted for arrays used in a wire number scan [35] on the SATURN generator ($16\times30\,\mu$m, $24\times25\,\mu$m, $32\times20\,\mu$m, $64\times15\,\mu$m, and $136\times10\,\mu$m wires). Whilst the total mass of the arrays was held roughly constant, the current per wire varied by a factor of 8.5. The results show that the amount of core material transferred to the corona and the corona expansion velocity were both weak functions of the number of wires. As a result, with fewer wires, the higher current per wire results in higher temperatures, sound speeds and Alfvén velocities in the corona. Therefore, with fewer wires, the $m=0$ activity is higher and the instability reaches sufficient nonlinear development for penetration of the wire core to occur prior to implosion [compare Figs. 10(b) and 10(c)]. Since at the start of implosion the vast majority of the mass remains in the wire cores, there is a substantial difference in $m=0$ perturbation amplitude between cases where the instability occurs in the corona only compared to cases where the instability penetrates the core. Consequently one would expect lower seed levels for the magneto-Rayleigh-Taylor instability and hence shorter x-ray pulse rise times and higher x-ray powers for larger numbers of wires. In simulation, the transition in perturbation amplitude occurs for this wire number scan between 32 and 48 wires, which is coincident with the experimentally observed transition in x-ray power at ~40 wires for 8.6 mm radius arrays [1,35].

Experimental observations [15] and simulations [19] in the r-θ plane both indicate that the coronal plasma is continuously swept away from the wire cores and injected into the interior of the array in the form of radial plasma streams. This mass injection again acts as an x-ray pulse broadening mechanism as the final implosion must compress a distributed radial density profile before reaching the axis. Expansion of the plasma coronas from each wire results in an early merger of this low-density material in the interwire gap. However, this merger cannot prevent mass injection as the $\mathbf{j}\times\mathbf{B}$ force rapidly accelerates this low density material between the wires into interior of the array. If, however, merger of higher density material occurs, then the injection of material is slower. The plasma density (or more appropriately the mass per unit length along the circumference) at the midpoint between wires is therefore a measure of the plasma merger and the anticipated level of mass injection. In the extreme case when the wire cores expand sufficiently to merge prior to implosion, then whilst some mass injection will occur prior to merger, the final implosion itself will be of a moderately uniform, high-density plasma shell. This contrasts with the strongly modulated azimuthal structure which occurs in wire array implosions where no significant merger occurs and the wires remain discrete.

The simulation results for the SATURN wire number scan indicate a general trend towards increasing plasma merger in the inter-wire gap and therefore increasing azimuthal uniformity with increasing numbers of wires. For example, for the 24 and 64 wire cases illustrated in Figs. 10(b) and 10(c), the mass per unit azimuthal length at the midpoint between the wires and at the start of implosion, is 3% and 10%, respectively of the average value one would obtain for a homogeneous plasma shell. The degree of plasma merger for 64 wires and above is probably sufficient to significantly reduce mass injection in the plasma formation phase and therefore results in the final implosion structure approaching that of a plasma shell.

It is interesting to note that in the simulation of a tungsten wire in an array on the Z generator [illustrated in Fig. 10(d)], despite substantial $m=0$ activity in the corona, the core has not been penetrated. The core diameter, however, is ~150 μm and remains much less than the interwire gap (524 μm for a 40 mm diameter array). The mass per unit azimuthal length at the midway point between the wires being 1.7% of the average. Thus whilst the wire number is sufficiently high to effectively reduce the MRT seed perturbation amplitude, it is not sufficient to eliminate mass injection in the r-θ plane and therefore this could well be the dominant x-ray pulse broadening mechanism in these experiments.

IX. DISCUSSION

By the addition of relatively simple models for the equations of state and dense plasma transport coefficients into a resistive MHD code, we have obtained a fair reproduction of experimental data for single metallic wire Z pinches. This is despite significant regimes of inaccuracy and uncertainty in both models. The sensitivity of the final results to the uncertainty in these models was examined by, for example, varying the resistivity in the condensed phase around 1 eV by an order of magnitude. These somewhat extreme changes re-

sulted in only modest variations (factors of 2) in the expansion velocities of corona and core with the qualitative results of persistence of the core/corona structure and the dominance of the $m=0$ instability remaining unchanged. One possible explanation for this apparent insensitivity may be that the periods over which these models have a strong influence are quite short.

The radial profiles of pressure in Fig. 3(b) indicate that after 25 ns, the plasma pressure is approximately matched by the perfect gas pressure even in the high-density core and therefore the complex equation of state model becomes redundant. The differences between the transport model and Spitzer-like behavior persist until later in the simulation. However, the vast majority of the current is flowing in the corona and the only significant application of the complex transport model is in determining the Ohmic heating rate in the core.

During the first few nanoseconds, volume heating of the wire material to its vaporization temperature is followed by the rapid formation, explosion and self pinching of a coronal plasma. During this phase a modified Thomas-Fermi model is required in order to correctly model the condensed phases in the wire core. Thereafter, the evolution of the pinch is consistent with that of a cold dense plasma expanding at the sound speed surrounded by a much hotter and lower density corona, which contains the current and is magnetically confined but $m=0$ unstable. The modeling of this phase could be approximated by a perfect gas equation of state and much simpler transport models.

The results are in fact more sensitive to inaccuracies in the treatment of the more ''conventional'' problem of radiation loss. The only substantial radiation emission from these pinches comes from the x-ray bright spots formed in the necks of the $m=0$ instability. However the radiation loss is also important in determining the electron temperature in the low density coronal plasma and therefore affects the expansion and instability development. The model described in Refs. [26] and [27], assumes complete transparency of the plasma and is strictly speaking only applicable for very low density plasmas. In practice, the majority of the pinch is optically thick to part of the line spectrum and therefore this model overestimates the radiative cooling.

The most significant discrepancy between simulation and single wire results presented here is the expansion and longevity of the aluminum wire core in the IMP experiment. Since Ohmic heating is the dominant mechanism in determining the core temperature, it is most likely that inaccuracy in the resistivity is responsible, particularly as the core plasma parameters are in the regime of greatest uncertainty. By decreasing the minimum electron mean free path used in Ref. [22] to less than the inter-atomic separation, the expansion of the core can be reduced. However, this is a somewhat arbitrary modification and is contrary to the findings of other authors [36] who obtain better fits to experimental data by

increasing this parameter. In addition, the core expansion predicted for low-current aluminum wires is, by contrast, too slow. Therefore, it is unlikely that a single simple modification can be used to improve the agreement between simulation and experiment over a wide range of parameters.

The nonlinear behavior of the $m=0$ instability experimentally observed in wires in an array is very different to that observed in single-wire experiments and to that simulated here. Work to include the equation of state and transport models described here into a 3D resistive MHD code is presently underway in order to provide more quantitative modeling of these experiments.

Simulations with similar conditions to wires in an array show a general trend in the plasma structure at the start of implosion from discrete wires with large $m=0$ perturbation amplitudes to partially merged wires with smaller perturbation amplitudes as the number of wires is increased. Results for a wire number scan with aluminum wire arrays on the SATURN generator suggest that the observed sharp transition to high x-ray power at around 40 wires corresponds to a sharp decrease in $m=0$ perturbation amplitude and hence a sharp decrease in the seed perturbation for the Rayleigh-Taylor instability.

The slower core expansion velocity in tungsten pinches compared to aluminum, means that for a 40 mm diameter array of 240, 7.5 μm tungsten wires on the Z generator [see Fig. 10(d)] significant mass injection and azimuthal modulation of the implosion structure is to be expected. Azimuthal modulation could be eliminated and a shell-like implosion structure obtained by using sufficient numbers of wires ($\sim$840) for merger of the wire cores to occur prior to implosion. A more practicable alternative would be the use of a pre-pulse current to expand the wire cores prior to the application of the main current pulse. After vaporizing, the wire cores expand at roughly their sound speed ($\sim$500 ms^{-1}) and would cross the interwire gap in $\sim$500 ns. Increasing the pre-pulse current does not significantly change this velocity but simply serves to heat the corona and therefore once the wires have been vaporized, the prepulse current serves little further purpose and can be switched off. Applying a slowly rising, low-amplitude current would result in negligible instability growth during the prepulse phase. Simulations using the model described above suggest that if a shell-like implosion is deemed necessary, it can be achieved by applying a prepulse current of $\sim$1 kA per wire over a 100 ns time scale and then waiting 500 ns before applying the main current pulse.

[1] T. W. L. Sanford, G. O. Allshouse, B. M. Marder, T. J. Nash, R. C. Mock, R. B. Spielman, J. F. Seamen, J. S. McGurn, D. Jobe, T. L. Gilliland, M. Vargas, K. W. Struve, W. A. Stygar, M. R. Douglas, M. K. Matzen, J. H. Hammer, J. S. De Groot, J. L. Eddleman, D. L. Peterson, D. Mosher, K. G. Whitney, J. W. Thornhill, P. E. Pulsifer, J. P. Apruzese, and Y. Maron, Phys. Rev. Lett. **77**, 5063 (1996).

[2] C. Deeney, T. J. Nash, R. B. Spielman, J. F. Seaman, G. C. Chandler, K. W. Struve, J. L. Porter, W. A. Stygar, J. S. McGurn, D. O. Jobe, T. L. Gilliland, J. A. Torres, M. F. Var-

gas, L. E. Ruggles, S. Breeze, R. C. Mock, M. R. Douglas, D. L. Fehl, D. H. McDaniel, M. K. Matzen, D. L. Peterson, W. Matuska, N. F. Roderick, and J. J. MacFarlane, Phys. Rev. E **56**, 5945 (1997).

[3] R. B. Spielman, C. Deeney, G. A. Chandler, M. R. Douglas, D. L. Fehl, M. K. Matzen, D. H. McDaniel, T. J. Nash, J. L. Porter, T. W. L. Sanford, J. F. Seamen, W. A. Stygar, K. W. Struve, S. P. Breeze, J. S. McGurn, J. A. Torres, D. M. Zagar, T. L. Gilliland, D. O. Jobe, J. L. McKenney, R. C. Mock, M. Vargas, T. Wagoner, and D. L. Peterson, Phys. Plasmas **5**, 2105 (1998).

[4] C. Deeney, M. R. Douglas, R. B. Spielman, T. J. Nash, D. L. Peterson, P. L'Eplattenier, G. A. Chandler, J. F. Seamen, and K. W. Struve, Phys. Rev. Lett. **81**, 4883 (1998).

[5] E. S. Figura, G. H. McCall, and A. E. Dangor, Phys. Fluids B **3**, 2835 (1991).

[6] D. Kalantar and D. Hammer, Phys. Rev. Lett. **71**, 3806 (1993).

[7] F. N. Beg, A. E. Dangor, P. Lee, M. Tatarakis, S. L. Niffikeer, and M. G. Haines, Plasma Phys. Controlled Fusion **39**, 1 (1997).

[8] S. V. Lebedev, R. Aliaga-Rossel, J. P. Chittenden, I. H. Mitchell, A. E. Dangor, M. G. Haines, and J. F. Worley, Phys. Plasmas **9**, 3366 (1998).

[9] G. V. Ivanenkov, A. R. Mingaleev, S. A. Pikuz, V. M. Romanova, T. A. Shelkovenko, W. Stepniewski, and D. A. Hammer, Zh. Eksp. Teor. Fiz. **114**, 1215 (1998) [JETP **87**, 663 (1998)].

[10] S. Y. Guskov, G. V. Ivanenkov, A. R. Mingaleev, S. A. Pikuz, T. A. Shelkovenko, and D. A. Hammer, Pis'ma Zh. Eksp. Teor. Fiz. **67**, 531 (1998) [JETP Lett. **67**, 559 (1998)].

[11] J. Ruiz-Camacho, F. N. Beg, A. E. Dangor, M. G. Haines, E. L. Clark, and I. Ross, Phys. Plasmas **6**, 2579 (1999).

[12] S. A. Pikuz, G. V. Ivanenkov, T. A. Shelkovenko, and D. Hammer, Pis'ma Zh. Eksp. Teor. Fiz. **69**, 349 (1999) [JETP Lett. **69**, 377 (1999)].

[13] C. Deeney, J. McGurn, D. Noack, J. L. Porter, R. B. Spielman, J. F. Seamen, D. O. Jobe, M. F. Vargas, T. Gilliland, M. R. Douglas, and M. K. Matzen, Rev. Sci. Instrum. **68**, 653 (1997).

[14] S. V. Lebedev, I. H. Mitchell, R. Aliaga-Rossel, S. N. Bland, J. P. Chittenden, A. E. Dangor, and M. G. Haines, Phys. Rev. Lett. **81**, 4152 (1998).

[15] S. V. Lebedev, R. Aliaga-Rossel, S. N. Bland, J. P. Chittenden, A. E. Dangor, M. G. Haines, and I. H. Mitchell, Phys. Plasmas **6**, 2016 (1999).

[16] I. K. Aivazov, V. D. Vikharev, G. S. Volkov, L. B. Nikandrov, V. P. Smirnov, and V. Ya. Tsarfin, Fiz. Plazmy **14**, 197 (1988) [Sov. J. Plasma Phys. **14**, 110 (1988)].

[17] C. Deeney, P. D. LePell, B. H. Failor, S. L. Wong, J. P. Apruzese, K. G. Whitney, J. W. Thornhill, J. Davis, E. Yadlowsky, R. C. Hazelton, J. J. Moschella, T. Nash, and N. Loter, Phys. Rev. E **51**, 4823 (1995).

[18] E. J. Yadlowsky, J. J. Moschella, R. C. Hazelton, T. B. Settersten, G. G. Spanjers, C. Deeney, B. H. Failor, P. D. LePell, J. Davis, J. P. Apruzese, K. G. Whitney, and J. W. Thornhill, Phys. Plasmas **3**, 1745 (1996).

[19] J. P. Chittenden, S. V. Lebedev, A. R. Bell, R. Aliaga-Rossel, S. N. Bland, and M. G. Haines, Phys. Rev. Lett. **83**, 100 (1999).

[20] M. G. Haines, IEEE Trans. Plasma Sci. **26**, 1275 (1998).

[21] J. P. Chittenden, R. Aliaga Rossel, S. V. Lebedev, I. H. Mitchell, M. Tatarakis, A. R. Bell, and M. G. Haines, Phys. Plasmas **4**, 4309 (1997).

[22] Y. T. Lee and R. M. More, Phys. Fluids **27**, 1273 (1984).

[23] A. R. Bell, Phys. Plasmas **1**, 1643 (1994).

[24] D. L. Youngs, in *Numerical Methods for Fluid Dynamics*, edited by K. W. Morton and M. J. Baines (Academic Press, New York, 1982).

[25] D. S. Kershaw, J. Comput. Phys. **26**, 43 (1978).

[26] C. B. Tarter, J. Quant. Spectrosc. Radiat. Transf. **17**, 531 (1977).

[27] D. E. Post, R. V. Jensen, C. B. Tarter, W. H. Grasberger, and W. A. Locke, At. Data Nucl. Data Tables **20**, 398 (1977).

[28] J. P. Chittenden, Phys. Plasmas **2**, 1242 (1995).

[29] R. Latter, Phys. Rev. **99**, 1854 (1955).

[30] D. A. Kirzhnits, Sov. Phys. JETP **8**, 1081 (1959).

[31] J. P. Christiansen, D. E. T. F. Ashby, and K. V. Roberts, Comput. Phys. Commun. **7**, 271 (1974).

[32] *Electrical Resistivity Handbook*, edited by G. T. Dyos and T. Farrell (Peter Peregrinus Ltd., London, 1992).

[33] J. P. Chittenden, I. H. Mitchell, R. Aliaga-Rossel, J. M. Bayley, F. N. Beg, A. Lorenz, M. G. Haines, and G. Decker, Phys. Plasmas **4**, 2967 (1997).

[34] T. A. Shelkovenko, S. A. Pikuz, A. R. Mingaleev, and D. Hammer, Rev. Sci. Instrum. **70**, 667 (1999).

[35] T. W. L. Sanford, R. C. Mock, R. B. Spielman, M. G. Haines, J. P. Chittenden, K. G. Whitney, J. P. Apruzese, D. L. Peterson, J. B. Greenly, D. B. Sinars, D. B. Reisman, and D. Mosher, Phys. Plasmas **6**, 2030 (1999).

[36] A. Ng, D. Parfeniuk, P. Celliers, L. DaSilva, R. M. More, and Y. T. Lee, Phys. Rev. Lett. **57**, 1595 (1986).